Torque Estimation for Robotic Joint With Harmonic Drive Transmission Based on Position Measurements

Hongwei Zhang, Saleh Ahmad, and Guangjun Liu, *Senior Member, IEEE*

***Abstract*—Joint torque sensory feedback is an effective technique for achieving high-performance robot force and motion control. However, most robots are not equipped with joint torque sensors, and it is difficult to add them without changing the joint's mechanical structure. A method for estimating joint torque that exploits the existing structural elasticity of robotic joints with harmonic drive transmission is proposed in this paper. In the presented joint torque estimation method, motor-side and link-side position measurements along with a proposed harmonic drive compliance model, are used to realize stiff and sensitive joint torque estimation, without the need for adding an additional elastic body and using strain gauges to measure the joint torque. The proposed method has been experimentally studied and its performance is compared with measurements of a commercial torque sensor. The results have attested the effectiveness of the proposed torque estimation method.**

***Index Terms*—Harmonic drive transmission, joint torque estimation, torque control.**

I. Introduction

JOINT torque feedback (JTF) is predominantly considered as an effective technique for improving the performance of robot control in the robotics community [1]–[5]. It is not just that JTF facilitates in suppressing the effect of payload in motion control of robot manipulators, (e.g., [6]), it also considerably eases the necessity to model the link dynamics. Owing its application in the design of distributed control algorithms, for example [7], or collision detection and reaction algorithms, joint torque sensing is a valuable capability for robots. JTF is also valuable in force, compliance, and impedance control.

To implement JTF control schemes, the measurement or estimation of the torque transmitted by the transmission system is essential. One possible approach to implement such control schemes is to equip the robot with a multiaxis force/torque (F/T) sensor. When using a F/T sensor at the robot wrist, the estimation of joint torques requires additional calculations, and the results may be affected by computation delays and model errors [8].

Manuscript received April 12, 2014; revised January 18, 2015; accepted February 5, 2015. Date of publication March 4, 2015; date of current version April 2, 2015. This paper was recommended for publication by Associate Editor J. C. Koo and Editor B. J. Nelson upon evaluation of the reviewers' comments. This work was supported in part by a research grant from the Natural Sciences and Engineering Research Council and in part by the Canada Research Chair program. This paper was presented in part at the IEEE International Conference on Robotics and Automation, Karlsruhe, Germany, May 6–10, 2013.

The authors are with the Department of Aerospace Engineering, Ryerson University, Toronto, ON M5B2K3, Canada (e-mail: gjliu@ryerson.ca).

Color versions of one or more of the figures in this paper are available online at http://ieeexplore.ieee.org.

Digital Object Identifier 10.1109/TRO.2015.2402511

JTF control schemes may also be implemented through direct joint torque sensing, methods of which include, but not limited to, elastic-element-based joint torque sensors that are positioned at the output of a robot's joints. The torsional deformation of the elastic element can be measured by different methods, e.g., based on strain gauges, inductive sensors, optical sensors, or encoders. A torque sensing technique that relies on using optical sensors to measure the deformation of an elastic body that is placed after the reduction mechanism was proposed in [9] by Tsetserukou *et al.* and its spin-off in [10]. Kawakami *et al.* [11] used a linear encoder to measure the torsional deformation of an additional elastic body that is also placed after the reduction mechanism.

Built-in torque sensing is another method, proposed originally by Hashimoto *et al.* in [12] and subsequently improved by others [13]–[15], in which torsional compliance of the harmonic drive flexspline is utilized for torque sensing. It relies on strain gages that are directly cemented on the harmonic drive flexspline. The introduction of local torque ripple due to the elliptical shape of the wave generator in harmonic drive transmissions is one drawback associated with the built-in torque sensing method. The torque ripple depends on the position and deformation of the flexspline because of which the separation of torque signal from the local torque ripple is difficult [15]. Apart from the sensitivity of strain gauges to electrical noise and temperature changes, a drawback associated with strain-gauge-based torque sensors is the regular need of maintenance and tuning.

In recent years, compact high-resolution absolute position encoders become commercially available. Mounting an absolute position encoder at the link-side of robotic joints makes it possible to measure the torsional deformation of the harmonic drive. In this paper, a new joint torque estimation method based on a proposed harmonic drive compliance model is developed. The torsional deformation of the harmonic drive is measured using both motor-side and link-side encoders. Subsequently, the resulting measurement is used with the proposed harmonic drive model to estimate the joint torque. The proposed torque estimation method is effective and provides an economical way of torque estimation for robots with harmonic drives, as demonstrated experimentally in this paper. The proposed method has eliminated the need for adding an additional elastic body to measure the joint torque, as done in the other joint torque measurement methods that are reviewed above.

This paper is organized in the following manner. The setup used to experimentally validate the theoretical developments of this paper is presented in Section II-A. The harmonic drive

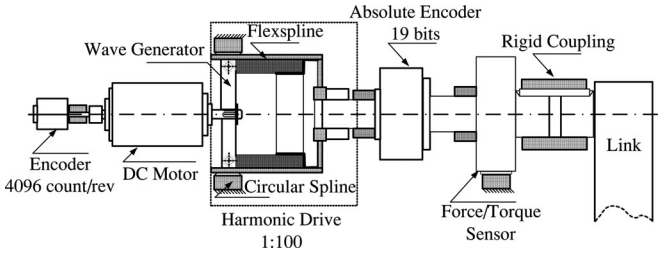

Fig. 1. Schematic diagram of the test-joint.

model is presented in Section II-B. The proposed torque estimation method is presented in Section III. Experimental results are given and discussed in Section IV. Two different control applications using the estimated joint torque are presented. Concluding remarks are given in Section V.

II. Harmonic Drive-Based Joint Design and Model

A. Harmonic Drive-Based Joint

To investigate the proposed joint torque estimation using position measurements, a robotic joint with harmonic drive and link-side encoder was developed at our laboratory. A schematic diagram of the developed joint is depicted in Fig. 1. The developed joint will be referred to as "test-joint" in the text to follow. The harmonic drive of the test-joint (model SHD-17-100-2SH) is driven by a brushed DC motor. The DC motor is instrumented with an optical incremental encoder with 4096 counts/rev to measure the rotor angular displacement. An absolute position encoder with 19-bit resolution is mounted on the link-side to measure the test-joint output angle. A commercial torque sensor is used to measure the load torque about the test-joint axis. The motor torque is obtained through the measured motor current.

B. Harmonic Drive Model

In order to estimate the joint torque based on position measurements, a harmonic drive compliance model is required. The goal of the proposed modeling strategy was not to develop a precise and possibly complicated compliance model but to generate an appropriate model that adequately reflect the compliance behavior of harmonic drives. In the test-joint used in the experimental setup, the wave generator is connected to the motor shaft, the circular spline is connected to the test-joint housing, and the flexspline is connected to the test-joint output. The kinematic relations that govern the harmonic drive transmission, nonlinear compliance, hysteresis behavior, and kinematic error are modeled as described next.

1) Harmonic Drive Kinematic Model: The angular positions at the components of the harmonic drive, as explained in [16], can be obtained by using the input/output kinematic relationship as

$$\theta_{wg} = N\theta_{fs} \tag{1}$$

where θ_{wg} is the wave-generator angular position, N is the gear ratio, and θ_{fs} is the flexspline output position. The static force balance between the elements can be described by

$$\tau_{wg} = \frac{1}{N}\tau_{fs} \tag{2}$$

where τ_{wg} is the torque at wave generator and τ_{fs} is the flexspline output torque. In (1) and (2), the harmonic drive transmission is treated as a perfectly rigid gear-reduction mechanism. However, empirical measurements of the input/output relationship do not yield a linear relationship between the input and output [13], [17]–[19]. The nonlinearity stems from torsional compliance in the harmonic drive components, nonlinear friction forces, and the kinematic error. The nonlinear kinematic relationship can be described by introducing compliance, friction, and kinematic error in the ideal kinematic relationship of the harmonic drive. The kinematic error is defined as the measured flexspline output minus the expected flexspline output (wave generator displacement multiplied by the gear ratio) [19]. Therefore, the kinematic error $\tilde{\theta}$ can be expressed as

$$\tilde{\theta} = \theta_{fsi} - \frac{\theta_{wgo}}{N} \tag{3}$$

where θ_{fsi} and θ_{wgo} denote the angular position at the flexspline gear toothed circumference and the angular position of the wave generator outside part (i.e., ball-bearing outer rim), respectively. If the harmonic drive frictional loss is considered, the expression in (2) becomes

$$\tau_{wg} = \frac{1}{N}(\tau_{fs} - \tau_{f_t}) \tag{4}$$

where τ_{f_t} is the harmonic drive lumped friction torque as seen with respect to the output side of the transmission. A number of previous research works on the compliance behavior of harmonic drives indicates that in addition to the well-known torsional compliance exhibited by flexspline, significant torsional deformation also occurs radially in the wave generator as well [17], [20]. In spite of its significance, the wave generator compliance received scant attention in the harmonic drive modeling literature. Most publications on harmonic drive modeling model this compliance behavior with a single stiffness element at the flexspline. The flexspline damping effect is considered in [21]–[23]. A novel model for torsional compliance and hysteresis behaviors in harmonic drives with consideration of the wave generator compliance was presented in [24] and [25]. In this model, the hysteresis behavior of the harmonic drive is captured by taking the torsional compliance of the wave generator into account. The model presented in this paper is an improved version of the one developed earlier by our research group as reported in [24], with kinematic error taken into account in the present model. The flexspline damping effect was not considered in this model as it is negligible at low to moderate joint motion speeds. Fig. 2 illustrates the compliance behavior of harmonic drives when the flexspline and wave generator compliance are considered. In Fig. 2, θ_{fso} denotes the flexspline angular position at the load side, a quantity measured using the link-side encoder; and θ_{wgi} denotes the angular position of the wave generator center part (i.e., the wave generator plug). The angles θ_{fso} and θ_{wgi} are measured by the link-side encoder and the motor-side encoder, respectively. The locations of these

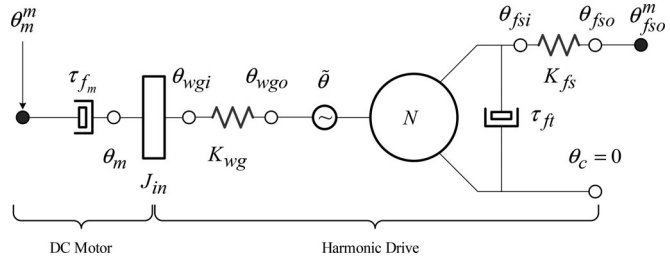

Fig. 2. Schematic illustration of the test-joint showing harmonic drive compliance components and sensor locations.

aforementioned measurement are denoted by θ_m^m and θ_{fso}^m, respectively. K_{wg} and K_{fs} denote the local elastic coefficient for the wave generator and the flexspline, respectively.

The torsional angle of the flexspline is defined as

$$\triangle\theta_{fs} = \theta_{fso} - \theta_{fsi}. \tag{5}$$

The wave-generator torsional angle is defined as

$$\triangle\theta_{wg} = \theta_{wgo} - \theta_{wgi}. \tag{6}$$

Note that θ_{fsi} and θ_{wgo} are unknown due to the fact that only the angles θ_{fso} and θ_{wgi} are measured by the link-side encoder and the motor-side encoder, respectively. The total torsional angle of the harmonic drive can be determined by

$$\triangle\theta = \theta_{fso} - \frac{\theta_{wgi}}{N}. \tag{7}$$

Substituting (3), (5), and (6) into (7) yields

$$\triangle\theta = \triangle\theta_{fs} + \frac{\triangle\theta_{wg}}{N} + \tilde{\theta}. \tag{8}$$

2) Harmonic Drive Compliance Model: A typical harmonic drive hysteresis curve is shown in Fig. 3(a), which features the harmonic drive hysteretic behavior [16]. As described in Section II-B1, the aggregate flexspline and wave generator deformation makes up the total harmonic drive torsional deformation. The compliance behavior of harmonic drive components, namely, the flexspline and wave generator compliance, were modeled in our previous work on harmonic drives modeling [25], [26]. As indicated in the experimental results obtained by Tuttle [17] and Kircanski and Goldenberg [18], wave generator deformation takes place at low applied torques. This is due to the fact that the wave generator stiffness increases sharply as the applied torque is increased. Based on this observation, the flexspline stiffness is determined by the slope of the curve obtained from stiffness data collected during the loading or the unloading of the harmonic drive with locked wave generator. In manufacturer's Catalog [16], a piecewise linear approximation method is used for modeling the flexspline compliance, where three straight lines were fit to the portion of the stiffness data collected during harmonic drive loading [see Fig. 3(b)]. The piecewise linear approximation has discontinuity and is not accurate as the curve was approximated by straight lines. Therefore, a more accurate flexspline compliance model is needed, and a proposed flexspline compliance model is described next.

As indicated in Fig. 3(b), the local elastic coefficient increases with the increase of τ_{fs}. Let us define the local elastic coefficient

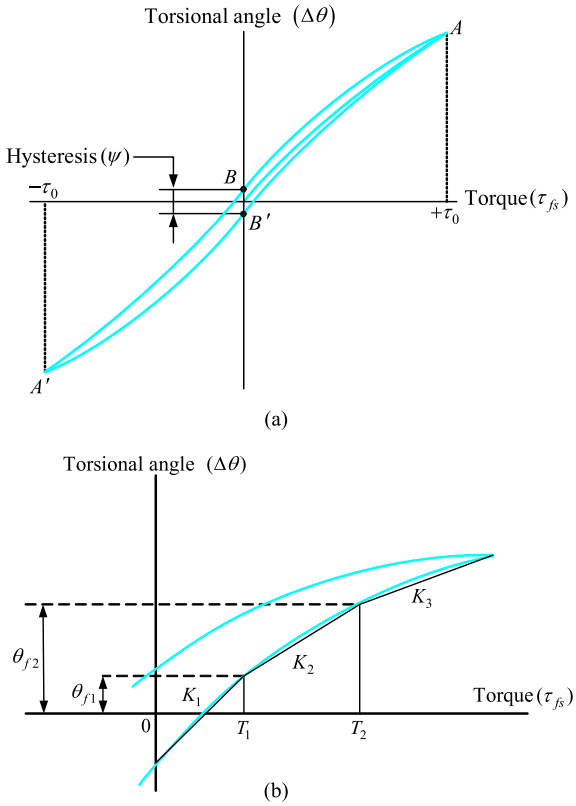

Fig. 3. Typical hysteresis curve of a harmonic drive. (a) Hysteresis curve. (b) Straight lines approximation of the flexspline stiffness.

as

$$K_{fl} = \frac{d\tau_{fs}}{d\Delta\theta_{fs}}. \tag{9}$$

Considering the symmetry property of the flexspline stiffness and using Taylor expansion, the local elastic coefficient is approximated by

$$K_{fl} = K_{fs0}(1 + (C_{fs}\tau_{fs})^2) \tag{10}$$

where K_{fs0} and C_{fs} are constants determined based on the harmonic drive datasheet parameters. Then, the flexspline torsion can be calculated as

$$\Delta\theta_{fs} = \int_0^{\tau_{fs}} \frac{d\tau_{fs}}{K_{fl}}. \tag{11}$$

Substituting K_{fl} of (10) into (11), we obtain

$$\Delta\theta_{fs} = \frac{\arctan(C_{fs}\tau_{fs})}{C_{fs}K_{fs0}} \tag{12}$$

where arctan(.) is the arctangent function. As shown in Fig. 3(a), the harmonic drive torsional deformation can range from $-\Psi/2$ to $\Psi/2$ at zero torque output, but drops down to zero at rated torque, where Ψ is the hysteresis loss. In order to replicate the hysteresis shape of this stiffness curve, the local elastic coefficient of wave generator is modeled as

$$K_{wg} = K_{wg0}e^{C_{wg}|\tau_{wg}|} \tag{13}$$

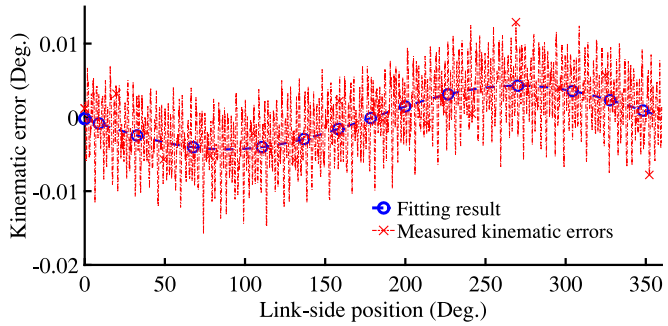

Fig. 4. Periodic fluctuations of the kinematic error with respect to one flexspline revolution.

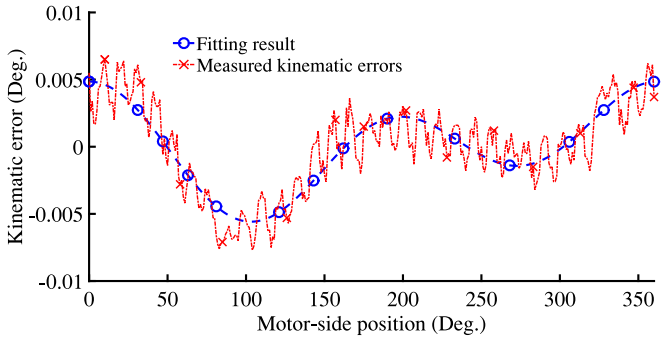

Fig. 5. Periodic fluctuations of the kinematic error with respect to one wave generator revolution.

where the value of the constants K_{wg0} and C_{wg} are determined experimentally.

The wave-generator's torsional angle can be calculated using

$$\triangle\theta_{wg} = \int_0^{\tau_{wg}} \frac{d_{\tau_{wg}}}{K_{wg}}. \tag{14}$$

Substituting (13) into (14), we obtain

$$\triangle\theta_{wg} = \frac{\text{sign}(\tau_{wg})}{C_{wg}K_{wg0}}(1 - e^{-C_{wg}|\tau_{wg}|}) \tag{15}$$

where sign(.) is the signum function. A detailed description, parameter estimation, and experimental validation of the proposed harmonic drive model can be found in [26].

3) Harmonic Drive Kinematic Error Model: Effective torque estimation requires compensation for the effects of the kinematic error. To proceed in this direction, a model of the harmonic drive kinematic error is developed as described below. To determine the kinematic error $\tilde{\theta}$, the test-joint is rotated clockwise and counterclockwise, one complete output revolution with no payload. The total torsional deformation $\triangle\theta_{cw}$ and $\triangle\theta_{ccw}$ are measured during this process. From (8)

$$\triangle\theta_{cw} = \triangle\theta_{fs} + \frac{\triangle\theta_{wg_{cw}}}{N} + \tilde{\theta}$$

$$\triangle\theta_{ccw} = \triangle\theta_{fs} + \frac{\triangle\theta_{wg_{ccw}}}{N} + \tilde{\theta}$$

where $\triangle\theta_{wg_{cw}}$ and $\triangle\theta_{wg_{ccw}}$ are the wave-generator torsional deformation in the clockwise and counterclockwise direction, respectively. Since the output torque is equal to zero, the flexspline torsional deformation is also equal to zero, $\triangle\theta_{fs} = 0$. With the assumption that the torsional deformation of the wave generator is symmetric, i.e.,

$$\triangle\theta_{wg_{cw}} = -\triangle\theta_{wg_{ccw}}$$

then, the kinematic error can be determined from

$$\tilde{\theta} = (\triangle\theta_{cw} + \triangle\theta_{ccw})/2.$$

Fig. 4 shows the periodic fluctuations of the kinematic error with respect to a complete flexspline revolution, while Fig. 5 shows the periodic fluctuations of the kinematic error for a complete wave generator revolution. Note that the kinematic error is measured for a constant wave generator velocity for both cases. Experimentally obtained waveform of kinematic error is

TABLE I
KINEMATIC ERROR MODELING PARAMETERS

Parameters	Value
a_0	0
a_{l1}	−0.0001476
b_{l1}	−0.004309
w_l	0.01731
a_{w1}	0.001594
b_{w1}	−0.001891
a_{w2}	0.003288
b_{w2}	0.0009049
w_w	0.01734

modeled using a general periodic form represented by finite Fourier series as in [14] and[27], and the obtained mathematical models of the motor-side and link-side kinematic error are given as

$$\begin{aligned}\tilde{\theta}_{wg} = {} & a_{wg0} + a_{wg1}\cos(\theta_{wgi}w_w) + b_{wg1}\sin(\theta_{wgi}w_w) \\ & + a_{wg2}\cos(2\theta_{wgi}w_w) + b_{wg2}\sin(2\theta_{wgi}w_w)\end{aligned} \tag{16}$$

$$\tilde{\theta}_l = a_{l0} + a_{l1}\cos(\theta_{fso}w_l) + b_{l1}\sin(\theta_{fso}w_l). \tag{17}$$

The fitting results for the link-side and motor-side kinematic errors are shown in Figs. 4 and 5, respectively. Finally, the total kinematic error is modeled as

$$\begin{aligned}\tilde{\theta} = {} & a_0 + a_{l1}\cos(\theta_{fso}w_l) + b_{l1}\sin(\theta_{fso}w_l) \\ & + a_{wg1}\cos(\theta_{wgi}w_w) + b_{w1}\sin(\theta_{wgi}w_w) \\ & + a_{wg2}\cos(2\theta_{wgi}w_w) + b_{w2}\sin(2\theta_{wgi}w_w)\end{aligned} \tag{18}$$

where the coefficients a_0, a_{l1}, b_{l1}, w_l, a_{wg1}, a_{wg2}, b_{wg1}, b_{wg2}, and w_w are obtained using the experimentally obtained waveform presented in Figs. 4 and 5. The values of these coefficients are summarized in Table I.

The obtained kinematic error model was implemented in *MATLAB*, and the output is shown in Fig. 6. The obtained kinematic error model is in agreement with the results obtained by Taghirad and Belanger [13] and Tuttle [17], which revealed that the kinematic error varies periodically at frequencies that are multiples of the wave-generator rotational velocity.

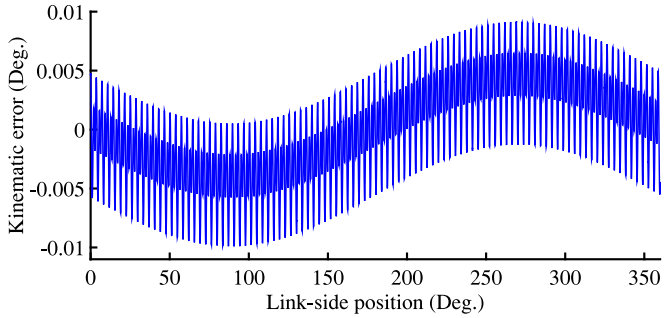

Fig. 6. Kinematic error model output.

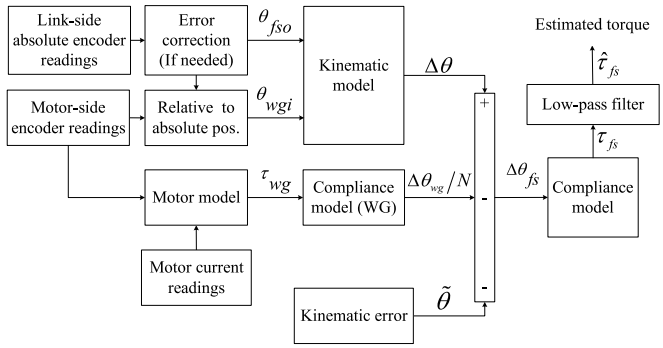

Fig. 7. Block diagram of the proposed torque estimation method.

III. Torque Estimation Method

Once an adequate compliance model is available, the joint torque can be estimated as described next. The compliance of the harmonic drive components was modeled in Section II-B2. By combining (8) and (15), one has

$$\triangle\theta_{fs} = \triangle\theta - \frac{\text{sign}(\tau_{wg})}{C_{wg}NK_{wg0}}(1 - e^{-C_{wg}|\tau_{wg}|}) - \tilde{\theta}. \quad (19)$$

The total torsional deformation of the harmonic drive $\triangle\theta$ is available through encoder measurements. The kinematic error $\tilde{\theta}$ was modeled in Section II-B3, and is given in (18). The wave generator torque τ_{wg} is estimated using the motor torque, which will be described later in this section.

After having the flexspline torsional deformation, $\triangle\theta_{fs}$, in hand, the joint torque estimate is obtained by inverting (12) as

$$\tau_{fs} = \frac{\tan(\triangle\theta_{fs}C_{fs}K_{fs0})}{C_{fs}}. \quad (20)$$

The proposed torque estimation method is illustrated by the block diagram in Fig. 7. In the test-joint, the motor current is measured using the motor-driver current sensing capability. The wave generator torque τ_{wg} can be estimated using the motor torque as

$$\tau_m = J_{\text{in}}\ddot{\theta}_{wg} + \tau_{f_m} + \tau_{wg} \quad (21)$$

where J_{in} denotes the combined inertia of the DC motor's rotor, shaft, and wave generator; τ_m denotes the motor torque, and τ_{f_m} denotes the motor friction. The term $J_{\text{in}}\ddot{\theta}_{wg}$ is small and can be ignored. Therefore, (21) can be rewritten as

$$\tau_{wg} = \tau_m - \tau_{f_m}. \quad (22)$$

To appropriately compensate the motor friction in (22), the following scenarios have to be considered. When the driving torque across the wave generator is in the same direction to the transmission velocity, both the load and the motor friction are working against the motor. However, when the driving torque becomes in the opposite direction to the transmission velocity, both the motor torque and the friction will be in the same direction. In this case, the friction must be added to the motor torque. The following equation describes the wave generator torque estimation:

$$\begin{cases} \text{if} \quad \dot{\theta}_{wgi}(t) > \epsilon, \quad \text{then} \\ \quad \begin{cases} \text{if} \quad \tau_m(t) > \tau_{f_m}, & \tau_{wg}(t) = \tau_m(t) - \tau_{f_m}; \\ \text{if} \quad \tau_m(t) < -\tau_{f_m}, & \tau_{wg}(t) = \tau_m(t) + \tau_{f_m}; \\ \text{if} \quad -\tau_{f_m} < \tau_m(t) < \tau_{f_m}, & \tau_{wg}(t) = \frac{\tau_{fs}(t)}{N}. \end{cases} \\ \text{if} \quad \dot{\theta}_{wgi}(t) < -\epsilon, \quad \text{then} \\ \quad \begin{cases} \text{if} \quad \tau_m(t) < -\tau_{f_m}, & \tau_{wg}(t) = \tau_m(t) + \tau_{f_m}; \\ \text{if} \quad \tau_m(t) > \tau_{f_m}, & \tau_{wg}(t) = \tau_m(t) - \tau_{f_m}; \\ \text{if} \quad -\tau_{f_m} < \tau_m(t) < \tau_{f_m}, & \tau_{wg}(t) = \frac{\tau_{fs}(t)}{N}. \end{cases} \\ \text{else}, \quad \tau_{wg}(t) = \tau_{wg}(t-1) \end{cases} \quad (23)$$

where ϵ is a small positive constant selected based on the magnitude of the velocity signal noise.

IV. Experimental Results

A. Joint Torque Estimation Experimental Results

This section provides the experimental results of testing the effectiveness of the proposed joint torque estimation method. Four different experiments were performed, in which the estimated joint torque was compared with the torque measurement from the F/T sensor. The experimental setup used to conduct the experimental verification is shown in Fig. 8. The physical parameters of the experimental setup and the coefficients used with the harmonic drive compliance model are given in Table II. A detailed description of how to determine the coefficients of the harmonic drive compliance model is presented in [26]. The discrete-time implementation and the parameters of the low-pass filter shown in Fig. 7 are given by: $\hat{\tau}_{fs}[i] = 0.95\hat{\tau}_{fs}[i-1] + 0.025\tau_{fs}[i] + 0.025\tau_{fs}[i-1]$, where $\hat{\tau}_{fs}$ is the filtered torque estimate, and τ_{fs} is the estimated torque from the model and readings of both encoders.

In the first experiment, the load torque was changed slowly by controlling the test-joint motion with a sinusoidal reference trajectory. The gradually changing load torque was introduced through moving links and joints driven by the test-joint. The torque estimate and the torque sensor output were recorded as a function of time, as depicted in Fig. 9. The maximum

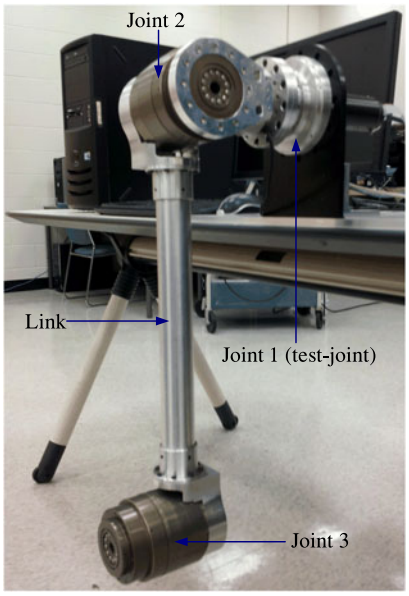

Fig. 8. Experimental setup.

TABLE II
PHYSICAL PARAMETERS OF THE EXPERIMENTAL SETUP AND HARMONIC DRIVE COMPLIANCE MODEL PARAMETERS

Physical parameters		
Parameter		Value
Rotor inertia for joint 1	(kg · m^2)	0.114×10^{-4}
Link mass	(kg)	0.641
Link length	(m)	0.45
Mass of joint 1 and 2	(kg)	1.2
Compliance model parameters		
Parameter		Value
K_{fs0}	(N·m/rad)	8.333×10^3
C_{fs}	(N·m^{-1})	0.089
K_{wg0}	(N·m/rad)	1.33
C_{wg}	(N·m^{-1})	83.5

difference between the estimated torque and the torque sensor measurement is 1.16 N·m, and the RMS level of the difference is 0.4061 N·m. In the second experiment, the results of which are depicted in Fig. 10, the load torque was changed rapidly by manually applying external torque in both directions. The maximum difference between the estimated torque and the torque sensor measurement for the second experiment is 1.8245 N·m, and the RMS level of the difference is 0.445 N·m. In the third experiment, a 10-N weight is attached to the link by a wire at a distance of 400 mm from the first joint axis. In the last experiment, the results of which are shown in Fig. 11, the test-joint is controlled to keep its position constant and the load was released suddenly by cutting the wire. This strategy was driven by the intention of verifying the response of the proposed torque estimation method to sudden payload changes. The difference between the torque estimate and the measurement of the torque sensor shown in Fig. 11 is caused by the unmodeled part of the joint friction. The reverse in the error direction after the sudden removal of the load is

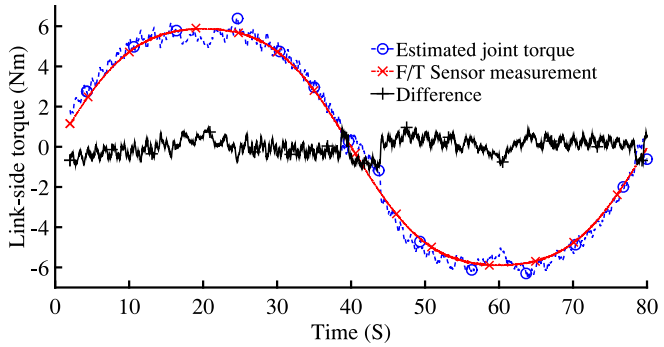

Fig. 9. Estimated torque versus torque measured by F/T sensor (response to slow changes).

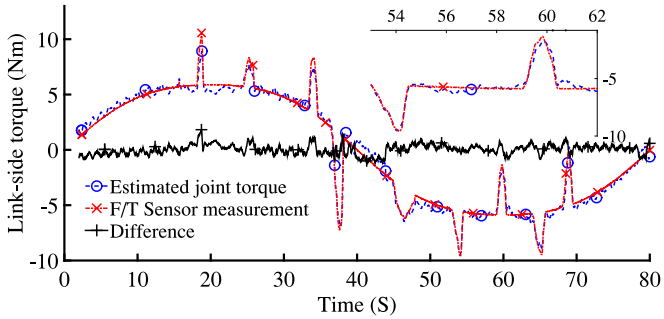

Fig. 10. Estimated torque versus torque measured by F/T sensor (response to fast changes).

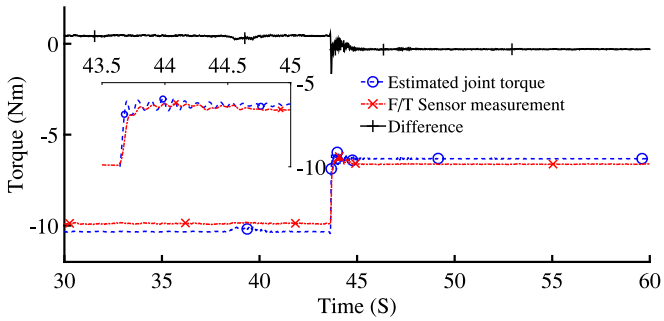

Fig. 11. Estimated torque versus torque measured by F/T sensor (response to sudden payload changes).

produced by a change in the friction torque that is caused by small joint movement. Since friction is position dependent, the error direction could reverse but never exceeded 0.5 N·m. In the fourth experiment, external static torques were applied at the link-side of the test-joint. The test-joint was loaded to the rated torque limit of the harmonic drive (16 N·m). The result of this experiment is shown in Fig. 12, where the RMS level of the difference is 0.215 N·m. The significance of the proposed torque estimation method can be highlighted by comparing its performance with that of built-in torque sensors. Harmonic drives with built-in torque sensor have been used as the reduction mechanism in our modular and reconfigurable robot for many years [28], [29]. In the built-in torque sensor, strain gages are directly cemented on the flexspline. Large torque ripples are caused by the elliptical shape of the flexspline, gear meshing

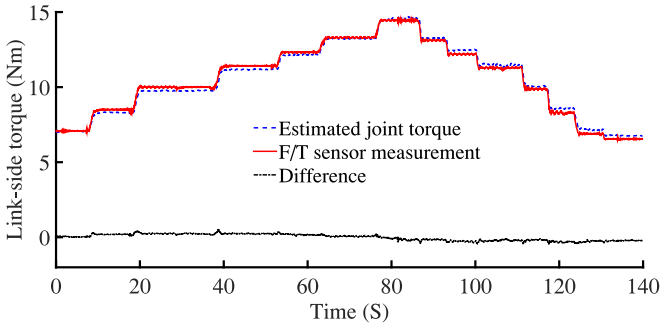

Fig. 12. Estimated torque versus torque measured by F/T sensor (static torque evaluation).

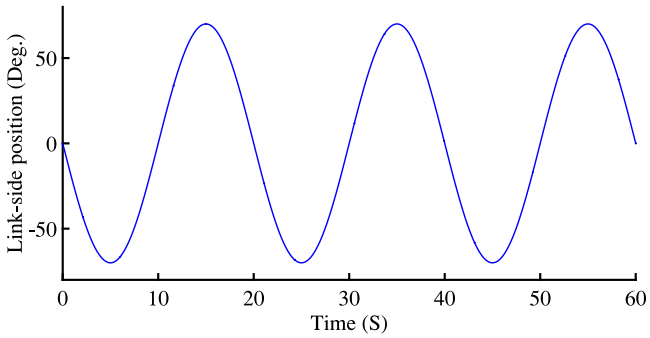

Fig. 13. Desired trajectory for active motion control.

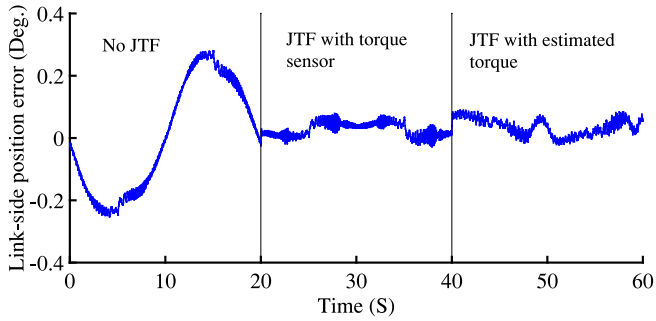

Fig. 14. Motion control experimental results.

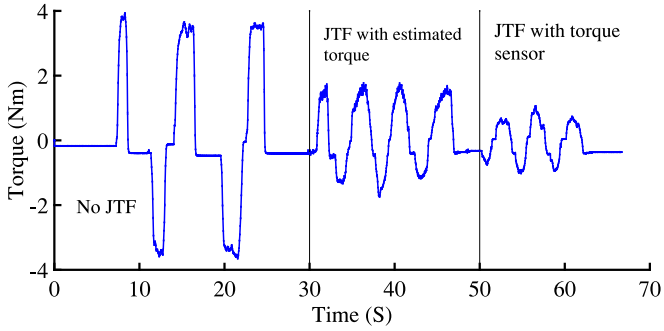

Fig. 15. Passive control experimental results.

vibration of the harmonic drive, and position inaccuracy of the strain gages [13]. Theoretically, the torque ripples can be compensated by a pair of strain gauges placed at 90° positions. However, torque ripples cannot be completely compensated as strain gauges cannot be cemented exactly on the required positions and with exactly required orientations due to limitations of the cementing techniques. In addition, individual strain gauges have slightly different gauge factors, which result in different amplitudes of the signal fluctuations from separate strain gauges [14]. Based on our experience, besides the undesirable torque ripples, built-in torque sensors also have the following drawbacks: Torque drift owing to the use of multiple amplifiers, and wiring faults can happen to the wires that connect the strain gages to the amplifier board. Built-in torque sensors typically have large torque ripples, the torque estimation also contains torque fluctuation but their magnitude is substantially smaller.

B. Motion Control With Joint Torque Feedback

The distributed control scheme with JTF presented in [3] is adopted in this paper as an application to demonstrate the effectiveness of the proposed joint torque estimation method. The experimental setup used to test this motion control scheme is shown in Fig. 8. Fig. 13 shows the desired trajectory for the test-joint, while the position tracking error of the motion control experiment is shown in Fig. 14. During the first 20 s of this experiment, no JTF was provided, while JTF from F/T sensor was applied during the subsequent 20 s. The position error when using JTF with estimated torque of the proposed method is shown in the last 20 s of the experiment time. The RMS values of the tracking error are 0.18, 0.035, and 0.045 for the cases when no JTF is used, JTF with the torque sensor, and JTF with the torque estimate, respectively. This results show 75% and 80% improvements when using JTF with the torque estimate and the torque sensor readings, respectively.

C. Passive Mode Control

In this section, the results of a passive mode control application based on JTF are presented. The control law used to implement the passive mode control is described in details in [30]. In the passive mode control, the external torque applied to the test-joint, which can be measured by the F/T sensor or estimated based on the proposed torque estimation method, is controlled to be around zero. Therefore, the test-joint will work in a passive mode, generating little resistance force. It should be noted that the friction at the motor and transmission systems tends to prevent the test-joint from moving freely. Thus, friction compensation is essential to enable the test-joint working in a free passive mode. As the magnitude of constant friction dominates the total friction at low speeds, the friction can be substantially compensated by applying a feedforward torque to the joint [29]. Integrating the friction compensation torque with a proportional controller gives the test-joint compensation torque. The experimental results, obtained when both of the estimated joint torque and the F/T sensor measurements are used as JTF for passive control, are shown in Fig. 15. The 70-s experimental time was broken down into three phases: First, when the test-joint was back-driven without JTF (the first 30 s period); second, when the JTF is applied using the estimated torque

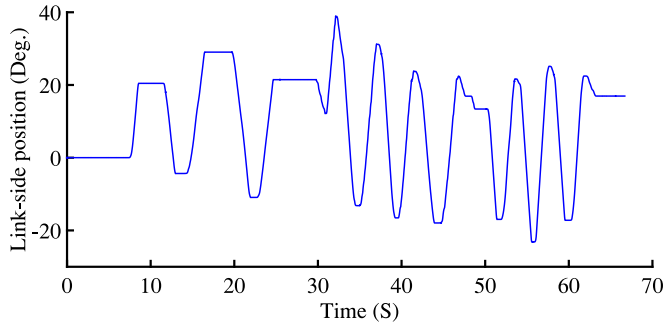

Fig. 16. Measured joint position for passive control.

(30–50 s period); and finally, when the JTF is applied using with the F/T sensor input (last 20 s). Note that the magnitude of the friction torque for the test-joint is relatively small, and the reduction in the magnitude when using JTF does not appear significant. In addition, as shown in Fig. 15, better result was achieved when using JTF with torque sensor because of lower noise in the sensor readings. From Fig. 15, the torque needed to back drive the test-joint when JTF was applied using the estimated torque is around 50%, which is less than the torque needed to back drive the test-joint with no JTF. When JTF was applied using F/T sensor measurements, the back-drive torque was around 75%, which is less than the torque with no JTF. The test-joint angular position during the passive control experiment is depicted in Fig. 16.

V. Conclusion

A novel joint torque estimation method based on position measurement and harmonic drive compliance model is presented in this paper. An advantage associated with the torque estimation using only position measurements is its immunity to noise. Using the torsional compliance of harmonic drive instead of an additional elastic component does not change the joint dynamics and simplify the joint mechanism design and build. Moreover, adding a link-side position sensor leads to the potential to improve joint control accuracy and reduce the cost of joint torque sensing. The estimated torque can find its applications in robotic control algorithms with JTF, as well as in collision detection/avoidance schemes.

Acknowledgment

The authors would like to thank Dr. Q. Zhang for performing the static torque estimation experiment and providing the test results that have been included in this paper.

References

[1] F. Aghili, M. Buehler, and J. M. Hollerbach, "Motion control systems with $\mathcal{H}^{\infty}$ positive joint torque feedback," *IEEE Trans. Control Syst. Technol.*, vol. 9, no. 5, pp. 685–695, Sep. 2001.

[2] F. Aghili and M. Namvar, "Adaptive control of manipulators using uncalibrated joint-torque sensing," *IEEE Trans. Robot.*, vol. 22, no. 4, pp. 854–860, Aug. 2006.

[3] G. Liu, S. Abdul, and A. Goldenberg, "Distributed modular and reconfigurable robot control with torque sensing," in *Proc. IEEE Int. Conf. Mechatron. Autom.*, Jun. 2006, pp. 384–389.

[4] W.-H. Zhu, E. Dupuis, and M. Doyon, "Adaptive control of harmonic drives," *ASME Trans. Dyn. Syst., Meas., Contr.*, vol. 129, no. 2, pp. 182–193, Aug. 2007.

[5] L. L. Tien, A. Albu-Schaffer, A. D. Luca, and G. Hirzinger, "Friction observer and compensation for control of robots with joint torque measurement," in *Proc. IEEE/RSJ Int. Conf. Intel. Robot. Syst.*, Sep. 2008, pp. 3789–3795.

[6] F. Aghili, J. Hollerbach, and M. Buehler, "A modular and high-precision motion control system with an integrated motor," *IEEE/ASME Trans. Mechatron.*, vol. 12, no. 3, pp. 317–329, Jun. 2007.

[7] G. Liu, S. Abdul, and A. A. Goldenberg, "Distributed control of modular and reconfigurable robot with torque sensing," *Robotica*, vol. 26, pp. 75–84, Jan. 2008.

[8] M. Randazzo, M. Fumagalli, F. Nori, L. Natale, G. Metta, and G. Sandini, "A comparison between joint level torque sensing and proximal f/t sensor torque estimation: Implementation on the iCub," in *Proc. IEEE/RSJ Int. Conf. Intel. Robot. Syst.*, Sep. 2011, pp. 4161–4167.

[9] D. Tsetserukou, R. Tadakuma, H. Kajimoto, and S. Tachi, "Optical torque sensors for implementation of local impedance control of the arm of humanoid robot," in *Proc. IEEE Int. Conf. Robot. Autom.*, May 2006, pp. 1674–1679.

[10] S. Shams, D. Shin, J. Han, J.-Y. Lee, K. Shin, and C.-S. Han, "Compact design of a torque sensor using optical technique and its fabrication for wearable and quadruped robots," in *Proc. IEEE/RSJ Int. Conf. Intel. Robot. Syst.*, Sep. 2011, pp. 5127–5132.

[11] T. Kawakami, K. Ayusawa, H. Kaminaga, and Y. Nakamura, "High-fidelity joint drive system by torque feedback control using high precision linear encoder," in *Proc. IEEE Int. Conf. Robot. Autom.*, May 2010, pp. 3904–3909.

[12] M. Hashimoto, Y. Kiyosawa, and R. Paul, "A torque sensing technique for robots with harmonic drives," *IEEE Trans. Robot. Autom.*, vol. 9, no. 1, pp. 108–116, Feb. 1993.

[13] H. Taghirad and P. Belanger, "Torque ripple and misalignment torque compensation for the built-in torque sensor of harmonic drive systems," *IEEE Trans. Instrum. Meas.*, vol. 47, no. 1, pp. 309–315, Feb. 1998.

[14] I. Godler, M. Horiuchi, M. Hashimoto, and T. Ninomiya, "Accuracy improvement of built-in torque sensing for harmonic drives," *IEEE/ASME Trans. Mechatron.*, vol. 5, no. 4, pp. 360–366, Dec. 2000.

[15] J. Sensinger and R. Weir, "Improved torque fidelity in harmonic drive sensors through the union of two existing strategies," *IEEE/ASME Trans. Mechatron.*, vol. 11, no. 4, pp. 457–461, Aug. 2006.

[16] H. D. Technologies, "CSD and SHD ultra-flat component sets and gearheads," Harmonic Drive Technologies, Peabody, MA, USA, 2012.

[17] T. Tuttle, "Understanding and modeling the behavior of a harmonic drive gear transmission," MIT Artificial Intelligence Laboratory, Cambridge, MA, USA, Tech. Rep. 1365, 1992.

[18] N. M. Kircanski and A. A. Goldenberg, "An experimental study of nonlinear stiffness, hysteresis, and friction effects in robot joints with harmonic drives and torque sensors," *Int. J. Robot. Res.*, vol. 16, no. 2, pp. 214–239, 1997.

[19] P. Curt, R. J. Thomas, and S. Deming, "A high-fidelity harmonic drive model," *ASME J. Dyn. Syst., Meas. Contr.*, vol. 134, no. 1, pp. 457–461, Apr. 2012.

[20] C. Kennedy and J. Desai, "Modeling and control of the mitsubishi pa-10 robot arm harmonic drive system," *IEEE/ASME Trans. Mechtron.*, vol. 10, no. 3, pp. 263–274, Jun. 2005.

[21] W.-H. Zhu, "Precision control of robots with harmonic drives," in *Proc. IEEE Int. Conf. Robot. Autom.*, Apr. 2007, pp. 3831–3836.

[22] A. Albu-Schäfer, and G. Hirzinger, "Parameter identification and passivity based joint control for a 7 dof torque controlled light weight robot," in *Proc. IEEE Int. Conf. Robot. Autom.*, May 2001, pp. 2852–2858.

[23] A. De Luca, R. Farina, and P. Lucibello, "On the control of robots with visco-elastic joints," in *Proc. IEEE Int. Conf. Robot. Autom.*, Apr. 2005, pp. 4297–4302.

[24] H. Zhang, S. Ahmad, and G. Liu, "Modeling of torsional compliance and hysteresis behaviors in harmonic drives," *IEEE/ASME Trans. Mechtron.*, vol. 20, no. 1, pp. 178–185, Feb. 2015.

[25] H. Zhang, S. Ahmad, and G. Liu, "Torque estimation technique of robotic joint with harmonic drive transmission," in *Proc. IEEE Int. Conf. Robot. Autom.*, May 2013, pp. 3034–3039.

[26] H. Zhang, "Development and multiple mode control of modular and reconfigurable robot," Ph.D. dissertation, Ryerson University, Toronto, ON, Canada, May 2013.

[27] P. Gandhi and F. Ghorbel, "Control of hysteresis and kinematic error nonlinearities in harmonic drives for high speed precision control applications," in *Proc. Amer. Control Conf.*, 2004, vol. 2, pp. 1141–1146.
[28] G. Liu, X. He, J. Yuan, S. Abdul, and A. Goldenberg, "Development of modular and reconfigurable robot with multiple working modes," in *Proc. IEEE Int. Conf. Robot. Autom.*, May 2008, pp. 3502–3507.
[29] S. Ahmad, H. Zhang, and G. Liu, "Multiple working mode control of door opening with a mobile modular and reconfigurable robot," *IEEE/ASME Trans. Mechatron.*, vol. 18, no. 3, pp. 833–844, Jun. 2013.
[30] H. Zhang, Y. Liu, and G. Liu, "Multiple mode control of a compact wrist with application to door opening," *Mechatronics*, vol. 23, no. 1, pp. 10–20, Feb. 2013.

Hongwei Zhang received the B.Sc. degree from University of Science and Technology of China, Hefei, China, in 1990; the M.E. degree from Tongji University, Shanghai, China, in 1993; and the Ph.D. degree from Ryerson University, Toronto, ON, Canada, in 2013.

His research interests include multiple working modes control design for modular and reconfigurable robots. His research also focuses on the precise modeling of harmonic drive transmission, taking into account the hysteresis properties, nonlinear friction dissipation, and kinematic error.

Saleh Ahmad received the B.Sc. degree in electronics engineering from Sebha University, Sebha, Libya, in 1999; the M.Sc. degree in control engineering from Lakehead University, Thunder Bay, ON, Canada, in 2008; and the Ph.D. degree from Ryerson University, Toronto, ON, in 2013.

From May 2013 to July 2014, he was a Postdoctoral Fellow with the Aerospace Engineering Department, Ryerson University. His research interests include harmonic drive modeling, mobile manipulation, and multiple working modes control design for modular and reconfigurable robots.

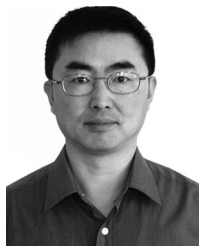

Guangjun Liu (M'99–SM'08) received the B.E. degree from University of Science and Technology of China, Hefei, China, in 1984; the M.E. degree from Chinese Academy of Sciences, Shenyang Institute of Automation, Shenyang, China, in 1987; and the Ph.D. degree from University of Toronto, Toronto, ON, Canada, in 1996.

From 1997 to 1999, he was a Systems Engineer and a Design Lead for Honeywell Aerospace Canada, where he was involved in the Boeing X-32 program. In 1996, he was a Postdoctoral Fellow with Massachusetts Institute of Technology, Cambridge, MA, USA. He is currently a Professor and the Canada Research Chair in Control Systems and Robotics with the Department of Aerospace Engineering, Ryerson University, Toronto, ON, Canada. He has authored or coauthored more than 170 papers in international journals and conference proceedings. His research interests include control systems and robotics, particularly in modular and reconfigurable robots, mobile manipulators, and aircraft systems.

Dr. Liu is a former Technical Editor of IEEE/ASME TRANSACTIONS ON MECHATRONICS and a licensed Member of the Professional Engineers of Ontario, Canada.